



Effect of heterogeneity of brittle rock on micromechanical extensile behavior during compression loading

Hengxing Lan,^{1,2} C. Derek Martin,¹ and Bo Hu¹

Received 27 March 2009; revised 14 August 2009; accepted 23 September 2009; published 26 January 2010.

[1] A grain-based Universal Distinct Element Code model was developed to generate a deformable polygonal grain-like structure to simulate the microstructure of brittle rock. It takes into account grain-scale heterogeneity including microgeometric heterogeneity, grain-scale elastic heterogeneity, and microcontact heterogeneity. The microgeometric heterogeneity can be used to match the grain size distribution of the rock. The discrete element approach is able to simulate the microheterogeneity caused by elastic variation and contact stiffness anisotropy. The modeling approach was evaluated using Lac du Bonnet granite and Äspö Diorite. The microheterogeneity played an important role in controlling both the micromechanical behavior and the macroscopic response when subjected to uniaxial compression loading. The crack-initiation stress was found to be controlled primarily by the microscale geometric heterogeneity, while the microcontact heterogeneity controlled the strength characteristics. The effect of heterogeneity on the distribution and evolution of tensile stresses and associated extension cracks was also examined.

Citation: Lan, H., C. D. Martin, and B. Hu (2010), Effect of heterogeneity of brittle rock on micromechanical extensile behavior during compression loading, *J. Geophys. Res.*, 115, B01202, doi:10.1029/2009JB006496.

1. Introduction

[2] Brittle rock is in nature a heterogeneous material which can be described by its internal microstructure. Micromechanical observations made during compression loading [Hallbauer *et al.*, 1973; Olsson and Peng, 1976; Kranz, 1983] have indicated that fracture initiation and fracture growth in brittle rock are to a large extent influenced by the presence of microstructure that introduces a heterogeneity in the stress distribution at the grain scale [Van de Steen *et al.*, 2003]. A key role of heterogeneity appears to be the creation of local concentrations of tensile stress, even when the rock as a whole is subjected only to compressive stress [Gallagher *et al.*, 1974; Blair and Cook, 1998a, 1998b]. It has been generally accepted by various studies that the processes of damage initiation, accumulation, and interaction are primarily tensile, with shear mechanisms becoming important only after sufficient tensile damage accumulation and interaction have occurred [Fairhurst and Cook, 1966; Brace *et al.*, 1966; Hallbauer *et al.*, 1973; Tapponier and Brace, 1976; Fonseka *et al.*, 1985; Martin and Chandler, 1994; Diederichs, 2003]. The tensile failure mechanism plays a strong role in the fracture mechanism in which the microtensile failure nucleate because of the local geometrical inhomogeneities of rock, propagate and eventu-

ally coalesce into macrofractures [Tapponier and Brace, 1976; Wong, 1982a, 1982b; Fredrich *et al.*, 1995; Wong *et al.*, 2006].

[3] At the grain-scale intact crystalline rock consists of a variety of mineral grains at different sizes. Mineral grains and associated contacts are two microstructural elements in addition to preexisting defects in the form of cracks and strings of grain boundary cavities. These features give rise to several types of microscopic heterogeneity: geometric heterogeneity resulting from angular shape and grain size, elastic heterogeneity due to the stiffness contrast of different grains, and contact heterogeneity resulting from the anisotropy of contact distributions (length and orientation) and stiffness anisotropy. The effects of these heterogeneities, however, have not been well understood, although the effect of grain size on the strength and deformation has been studied experimentally [Brace, 1961; Fredrich *et al.*, 1990; Wong *et al.*, 1996; Eberhardt *et al.*, 1999]. Since the heterogeneity in the microstructure is primarily due to the variation in grain size and shape [Blair and Cook, 1998a, 1998b; Zavattieri *et al.*, 2001], the grain size distribution in materials such as brittle rock may be a good index for representing the microheterogeneity. For example, Lac du Bonnet (LdB) granite is composed of approximately 40% K-feldspar, 20% plagioclase, 30% quartz, and 10% mafic minerals, mainly biotite. Although similar in mineral composition as LdB granite, the granodiorite exhibited a different behavior because its grain size distribution was more uniform [Martin *et al.*, 1997].

[4] The role of microscale tension cracking in compressive failure of brittle rock has been widely accepted. However, the effect of heterogeneity on the process of tensile stress

¹Department of Civil and Environmental Engineering, University of Alberta, Edmonton, Alberta, Canada.

²Also at LREIS, Institute of Geographic Sciences and Natural Resources Research, Chinese Academy of Sciences, Beijing, China.

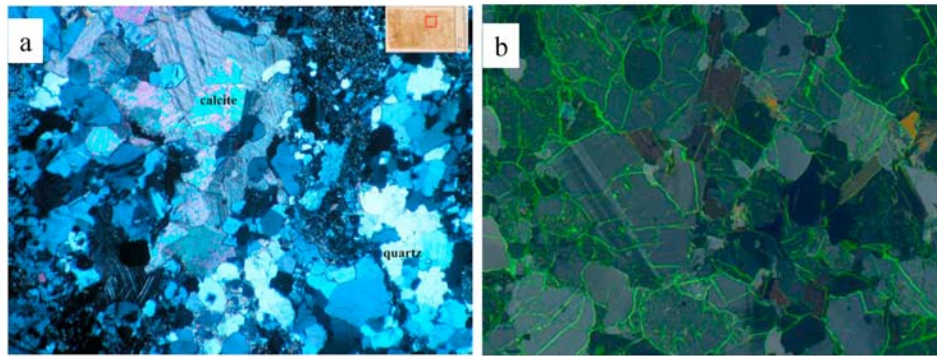


Figure 1. Example of the mineral grain structure observed in polarized light thin section. (a) Äspö Diorite (AD). Thick calcite blebs and veins that have typical calcite crystal twinning. Width of the image is 4 mm (modified from *Lampinen* [2006]). (b) Lac du Bonnet (LdB) granite. Combined polarized and fluorescent microscopic image of specimen from Underground Research Laboratory (URL) in Canada. Width of the image is 4 mm (modified from *Akesson* [2008]).

generation in terms of the tensile crack initiation, growth or accumulation, and interaction or coalescence has not been investigated. In this study, the microstructure of brittle rock was simulated using a grain-based micromechanical model that matched the mineral grain size distribution and associated angular grain shapes. The different types of micro-heterogeneities were characterized using this model, and their effect on controlling the microtensile behaviors of brittle rock and its macroscopic response was examined.

2. Grain-Based UDEC Model

2.1. Grain-Based Microstructural Model

[5] It is obvious that the grain structure in Figure 1 cannot be modeled exactly in any numerical model. To simulate this grain geometry, three options are available: (1) disk-shaped grains such as is commonly assumed in the discrete element code, such as Particle Flow Code [*Potyondy and Cundall*, 2004], (2) square-shaped element used in some finite element codes, such as RFPA2D [*Tang*, 1997], and (3) polygonal grains which is usually available through the Voronoi diagram generator. Geometrically, it appears that the polygonal structure may be more representative of the mineral structure observed in crystalline rock such as illustrated in Figure 1.

[6] The Voronoi tessellation technique has been well accepted for simulating the microstructure of materials [*Nygårds and Gudmundson*, 2002; *Zhang et al.*, 2005; *Li et al.*, 2006]. It uses a set of seeds to divide the space into polygonal Voronoi cells. However, the Voronoi generators adopted in many computer codes, such as Universal Distinct Element Code (UDEC, a 2-D numerical program based on the distinct element method (DEM) for discontinuum modeling), usually have a relatively uniform distribution of grain sizes due to the uniform distribution of their generating seeds [*Li et al.*, 2006]. It is worth noting that rocks usually have nonuniform grain size distribution which results in their own characteristic geometric heterogeneity. Therefore, a general Voronoi generator should have ability to generate a nonuniform size distribution and be capable of handling complex-shaped mineral grain.

[7] A general Voronoi tessellation logic was developed to mimic the grain size distribution in intact rock and associated angular grain shape (Figure 2). First a disk/particle packing algorithm was implemented to satisfy any size distribution. The disks are divided into groups on the basis of the mineral types. The diameter of disks in each group satisfies the statistical property of the grain size, e.g., the mean grain size. The number of disks required in each group is estimated by taking into account the specimen area, the range of particle size, and the percentage of particles passing a particular size. All the disks are located randomly and packed perfectly, i.e., very small porosity, in the specimen container. Different minerals comprising the specimen (rock) are illustrated in different gray scales.

[8] The point sets required for the Voronoi tessellation are provided by the center of each disk generated in the first step. The space for a specimen is partitioned into polygonal cells using the Voronoi generator. Two Voronoi generators were developed: (1) ordinary Voronoi and (2) power Voronoi. The points in the ordinary Voronoi generator have no weight or equal weight, and the polygonal cell of an input point p is the set of points which have a smaller distance to p than to any other points. The power Voronoi generator (also called Weighted Voronoi diagram) is very similar to the ordinary Voronoi generator, except each point is also given a weight. The cell of an input point p is the set of points that have a smaller weighted distance to p than to any other points. The power Voronoi tessellation will generate a better grain size distribution than the ordinary Voronoi tessellation, but it will generate more regular polygons particularly when dealing with a great number of particles. The ordinary Voronoi tessellation will generate more irregular grain shape with reasonable grain size distributions (Figure 3a). Since the grain in the real rock is complexly irregular, the ordinary Voronoi tessellation was used to generate a polygonal grain size distribution that is representative of both LdB granite (Figure 3a) and Äspö Diorite (AD) models (Figure 3b).

[9] The grain-based model (GBM) is able to handle any number of material grain types. The polygonal grain structure produced using GBM link grain size and grain type information in a logical fashion that can mimic the rock

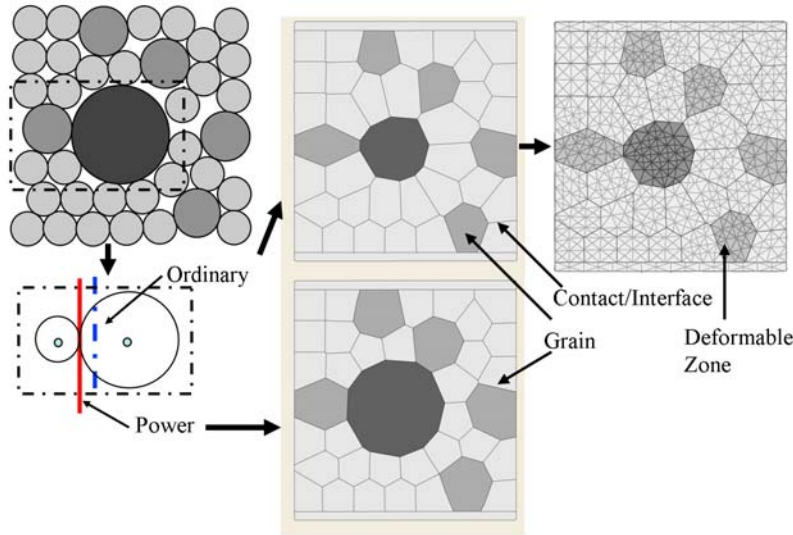


Figure 2. Grain-based micromechanical model using Voronoi diagram. It includes grains and the contact or interface between grains. Each grain is deformable by introducing triangular zones in numerical code such as UDEC.

microstructure. For many brittle rocks such as AD and LdB granite, four mineral grain types account for 90% or more of the mineral composition. The Voronoi models in Figure 3 were generated using four mineral types.

2.2. Numerical Approach

[10] *Cundall and Strack* [1979] showed how the discrete element method (DEM) could be used to simulate particle/soil behavior and *Potyondy and Cundall* [2004] showed how the same approach could be used to simulate rock behavior. The major advantage of the discrete element approach is that complex empirical constitutive behavior can be replaced with simple particle contact logic. In this context when the tensile or cohesive strength is exceeded, contacts between particles break. Once the bonds are broken, the displacement field in a discrete element formulation is controlled by particle geometry. This concept, while relatively simple, is quite important as it means that the failure process is not a predefined process as with the continuum modeling approach. But rather the failure process evolves progressively with each contact break leading to a redistribution of stress until a critical density of contact breaks exists that allows a rupture surface to propagate through the model.

[11] With the introduction of the bonded particle model (BPM) *Potyondy and Cundall* [1998] showed how discontinuum modeling could be used to simulate spalling, a form of stress induced failure observed around underground openings [*Fairhurst and Cook*, 1966]. The methodology was first applied to the Atomic Energy of Canada Ltd. (AECL)’s Mine-by Test Tunnel. While these early results were encouraging, calibrating the properties of the BPM to measured laboratory properties was highlighted as a major issue.

[12] More recently, *Cho et al.* [2007] demonstrated that some of these issues could be addressed by gluing the bonded particles into clumps. *Cho et al.* [2007] showed that once clumps were created the nonlinear failure envelope and the correct ratio of compressive strength-to-tensile strength were immediately recovered in the BPM. This discovery

implied that particle geometry played a more important role in controlling the behavior of the BPM than the contact properties themselves. Since the work of *Cho et al.* [2007], *Damjanac et al.* [2007] have shown that the same response obtained using a similar BPM clumped-logic in PFC2D (Particle Flow Code in two dimensions to model the move-

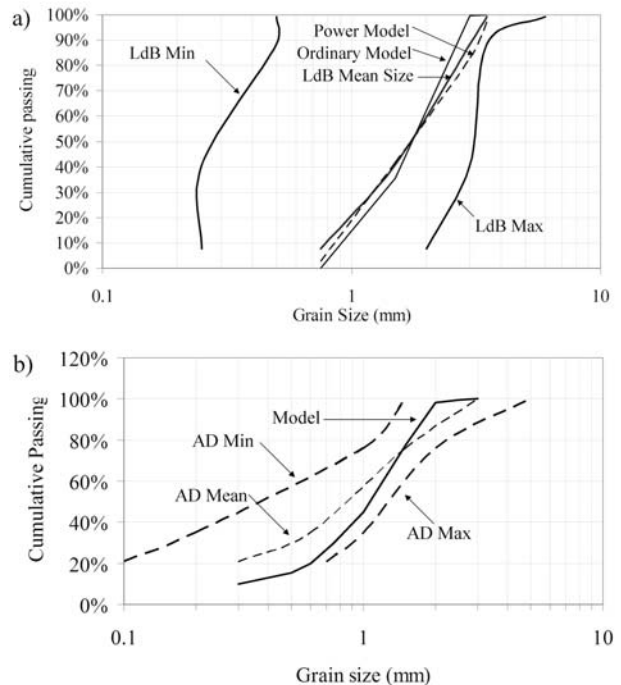


Figure 3. Grain size distribution of a sample of (a) LdB granite [*Kelly et al.*, 1994] and simulated grain size distribution using Ordinary Voronoi and Power Voronoi tessellation and (b) AD [*Lampinen*, 2006] and modeled grain size distribution using the Ordinary Voronoi tessellation.

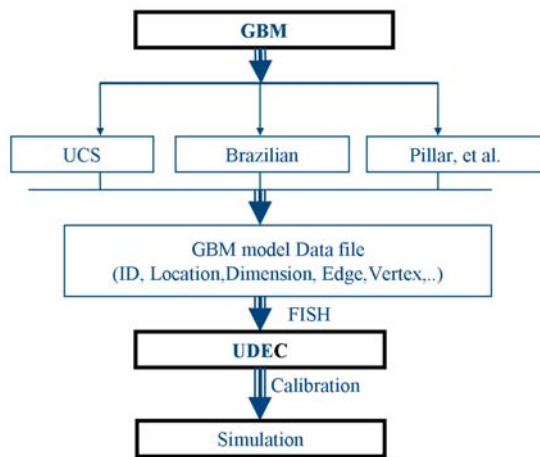


Figure 4. Procedure of generating a grain-based model in UDEC (GBM-UDEC).

ment and interaction of disc-shaped particles by the DEM) can be obtained using similar contact logic in UDEC.

[13] The application of UDEC to simulate the micro-mechanical response avoids the need for clumping as the voronoi tessellation scheme creates a polygonal structure similar to the clumps used by *Cho et al.* [2007]. The geometric model generated from the GBM is imported into UDEC via the edges and nodes information to mimic the microstructure of rock (Figure 4). Each grain has its unique identity (ID), location, and material type. All the information is exported to an ASCII file which can be imported into UDEC program using UDEC's internal macrolanguage FISH. The model geometry is created automatically in UDEC. Standard uniaxial compressive strength (UCS) test, Brazilian tensile test, and other complex test geometries can be created directly in UDEC. The grains are made deformable in UDEC by discretizing the interior of each polygon using triangular zones (see Figure 2). These deformable grains are cemented to one another along their adjoining sides, i.e., contacts or interfaces. At this stage of our research, the deformable grains are unbreakable. This has implications for the postpeak response but as noted by *Martin and Chandler* [1994] the prepeak response, particularly crack initiation and crack damage are not influenced by trans-granular cracking.

[14] Material properties are associated with the grains and interfaces. The statistical properties of the polygonal grain structure should be similar to those of rock being represented. Stiffness, cohesion, friction, and tensile strength are assigned to the boundaries of these polygonal blocks such that the macroscale strength is the same as the intact rock. Local variation in strength and stiffness can also be applied if required.

[15] A compression test in the GBM-UDEC is performed using an internal-based strain application scheme. It applies the axial-strain in a set of stages. Each stage consists of the following steps:

[16] 1. An axial-strain increment is applied to the system by setting the axial boundary velocity for a number of steps (for example, 5000 steps) at the start of the stage. A very low loading displacement rate will be applied at this stage, for example 10^{-5} m/s.

[17] 2. The compression is stopped by setting the boundary velocity to zero, and then the system is cycled until quasi-static equilibrium has been reached. All monitoring of stress and strain is limited to the middle one-third of the specimen.

3. Model Calibration

[18] The GBM-UDEC model was calibrated to the characteristic stress-strain response identified by *Martin and Chandler* [1994] for standard laboratory compression tests of intact rock.

3.1. UCS Model for LdB and AD

[19] Two UCS models were generated and calibrated to two types of brittle rocks: (1) LdB granite and (2) AD. LdB granite is the main rock type at AECL's Underground Research Laboratory (URL) near Winnipeg, Manitoba (Canada). AD is the dominant rock type found at SKB's (Swedish Nuclear Fuel and Waste Management Company) Äspö Hard Rock Laboratory (Sweden). Extensive studies have been carried out with respect to the characteristics and mechanical properties of these two rock types [*Martin and Chandler*, 1994; *Eberhardt et al.*, 1998; *Lajtai*, 1998; *Kelly et al.*, 1994; *Andersson*, 2007].

[20] Both rock types have similar mineral composition in which plagioclase, K-feldspar, and quartz are dominant, but with different grain size distribution (Figure 5). The mean grain size distribution of LdB granite is more uniform or equigranular than AD. Its mean size is nearly two times larger than AD, so a scaling factor was applied to AD in order to obtain a similar mean grain size as LdB granite (Figure 6).

[21] Figure 7 shows the configurations for the unconfined compression test for LdB granite and AD with the grain size distributions shown in Figure 6. The material is a rectangular specimen with a 125 mm height and 50 mm width. It comprises the four major minerals given in Figure 5. The strength heterogeneity resulting from the variant strength of different mineral types can be seen from the gray-scale distribution of the sample. The darker grains in models indicate the mineral types with higher strength such as Quartz.

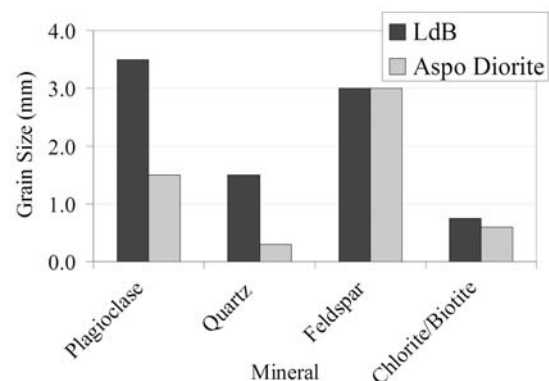


Figure 5. Mean grain size for LdB granite [from *Kelly et al.*, 1994] and AD [from *Lampinen*, 2006].

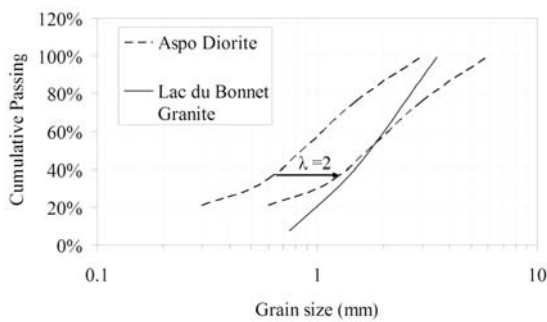


Figure 6. Comparison of grain size distribution between LdB granite and AD. The scaling factor $\lambda = 2$ is applied to the grain size distribution of AD in order to get similar mean grain size as LdB granite.

3.2. Calibration Scale

[22] In an effort to reduce the time required for the calibration of the microscale properties to match the macroscale response, a scale analysis was used (Figure 8). The GBM-UDEC sample was scaled to different sizes using the same grain size distribution. The same properties were assigned to each scaled sample for the UCS test. Figure 8 shows that stress-strain response from the different scaled samples behaves very similarly in the prepeak region. The dependency of postpeak response on the specimen size is in reasonable agreement with the findings of *Exadaktylos and Vardoulakis* [2001] who found that the postpeak strength decreases with increasing specimen size. The small-scaled sample was used to calibrate the elastic properties such as Young's modulus and Poisson's ratio to the laboratory properties. The contact normal stiffness and its ratio to shear stiffness play an important role during this calibration. The initial normal stiffness is set on the basis of the grain moduli and the distance of center of contacted grains, which is similar as the BPM model proposed by *Potyondy and Cundall*

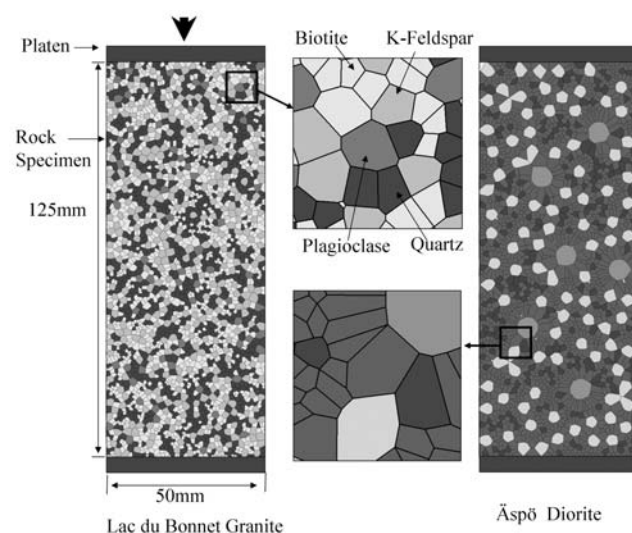


Figure 7. Layout for an unconfined compression test for a LdB granite and AD sample using GBM-UDEC model. The different gray scales indicate the degree of mineral grain strength. Higher strength grains have darker color.

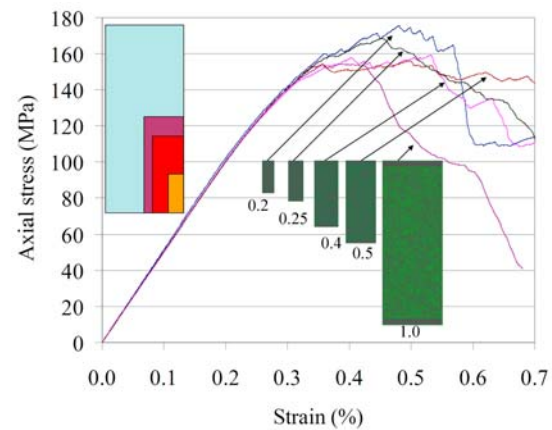


Figure 8. Result of scaling analysis for uniaxial compressive strength (UCS) test. The scaled samples have same grain size distribution.

[2004]. The calibrated properties are then assigned to the full-scale specimen. The other parameters such as friction are adjusted accordingly to match the peak strength of the laboratory sample.

3.3. Calibration Results

[23] The UCS laboratory test data for a sample of LdB granite taken from Cold Spring Quarry was used to calibrate the GBM-UDEC model of LdB granite. The UCS test KQ0064G01-6.26 [*Staub and Andersson*, 2004, R-04-01 at www.skb.se] was used to calibrate the GBM-UDEC model of AD.

[24] Since both models are composed of four mineral types, ten contact types were calibrated (Table 1) using the contact properties given in Table 2. A higher ratio of K_n (normal stiffness) to K_s (shear stiffness) was assigned to AD because it has more heterogeneous grain distribution. The mineral grain properties are shown in Table 3 on the basis of the published mineral experiments.

[25] Figure 9 shows the calibrated stress-strain response using the associated laboratory data in Table 2. The calibrated properties include Young's modulus, Poisson's ratio, and the three characteristic stress levels crack-initiation stress, crack damage stress, and peak stress defined by *Martin and Chandler* [1994]. The errors between the laboratory properties and the GBM-UDEC properties are within $\pm 5\%$. The ratio of crack-initiation stress and crack damage stress to peak stress in AD model are essentially the same (Table 4).

4. Effect of Grain-Scale Geometric Heterogeneity

[26] Both LdB granite and AD had similar geometric heterogeneity (see Figure 6). To investigate the effect of microgeometric heterogeneity on the microscopic mechanical behavior and associated macroscopic response, we conducted two geometric models (Figure 10): one is called microhomogenous model and another is microheterogeneous model.

[27] In model 1, all the interior grains have similar size and shape (homogenous model) whereas the interior grains in model 2 have various sizes and shapes (microheterogeneous model). Both models have similar mean grain size.

Table 1. Four Grain Types and Ten Interface Types^a

| Grain type | Plagioclase | Feldspar | Quartz | Biotite |
|-------------|-------------|----------|--------|---------|
| Plagioclase | 1 | 2 | 3 | 4 |
| K-Feldspar | | 5 | 6 | 7 |
| Quartz | | | 8 | 9 |
| Biotite | | | | 10 |

^aThe properties for the contact indices 1–10 are given in Table 2.

The same grain and contact properties are assigned to both models, so we can neglect the heterogeneity caused by variation of grain strength and contact properties. The heterogeneity of material is predominantly due to the grain morphology.

4.1. Macroscopic Response

[28] The macroscopic response of models 1 and 2 during uniaxial compression is compared in Figure 11. Both models exhibit similar response at the initial stage of the stress-strain response indicating elastic behavior, suggesting that both specimens can be presumed as homogeneous and linear elastic materials during the initial prepeak response. However, the stress-strain response for the heterogeneous model deviates significantly from that of the homogeneous model after an axial stress of about 125 MPa. Model 1 has much higher strength than model 2 due to its homogeneous grain size distribution. This suggests that the macroscopic stress-strain response, particularly the ultimate strength, is highly dependent on the heterogeneity induced by grain geometry and not the material properties.

[29] Cracking behaves distinctly differently in the two models. No microtensile cracks were observed in the homogeneous model 1. The initiation of microtensile crack occurs at the 0.32% strain in heterogeneous model 2 which corresponds to the crack-initiation stress level of 125 MPa which is about 47% of the peak strength of model 2 (264 MPa in this case). The microtensile cracks start growing dramatically at an axial strain of 0.5% indicating a stage of crack accumulation and coalescence. The crack-damage stress is 193 MPa about 73% of peak strength. While the homogeneous model might give similar macroscopic elastic constants as the laboratory properties, it is unable to determine the characteristic stress levels found in brittle rocks [Martin and Chandler, 1994].

Table 3. Moduli and Density of Common Minerals in Granite (from Bass [1995])

| ID | Mineral Type | Elastic Modulus and (K, G) ^a (GPa) | Poisson's Ratio | Density (g/cc) |
|----|-------------------------------|---|-----------------|-------------------|
| 1 | K-Feldspar | 69.8(53.7,27.2) | 0.28 | 2.56 |
| 2 | Plagioclase | 88.1(50.8,29.3) | 0.26 | 2.63 ^b |
| 3 | Quartz ^b | 94.5(37,44) | 0.08 | 2.65 |
| 4 | Biotite/chlorite ^b | 33.8(41.1,12.4) | 0.36 | 3.05 |

^a K , bulk modulus; G , shear modulus.

^bFrom Mavko *et al.* [2003]; chlorite is for AD.

4.2. Stress Distribution

[30] A study was also conducted using the two models to investigate the effect of geometric heterogeneity on the stress distribution within grains and along contacts. Blair and Cook [1998a, 1998b] indicated that local stress perturbations that result from grain-shape heterogeneity may have large effect on macroscopic properties. In these analyses, the minor principal stress distribution in the middle part of the models is examined, as it is not significantly affected by the boundary conditions (Figure 12).

[31] The minor principal stress is more uniformly distributed in the homogeneous model 1 than that in the heterogeneous model 2, particularly at 0.2% and 0.4% strain. Figure 13 shows the statistical analysis of the tensile stress developing along the grain contacts. Before an axial strain of 0.8%, there are no contacts existing in model 1 that are in tension. At an axial strain of 0.9%, less than 1% of the contacts in model 1 are in tension and most of these are located along the boundary where geometric heterogeneity is noticeable. In contrast, more than 20% of the contacts in model 2 have either cracked from tensile stresses or are under tension. Compared to model 2, the homogeneous grain geometry in model 1 has negligible effect on the generation of tension stresses whether within the grains or along their contacts. This suggests that geometric variation in grain size and shape induces the large tensile stress-field when a rock is subject to compressive stresses. Thus, the increasing local tensile stress heterogeneity resulting from the geometric heterogeneity has a dominant effect on tensile crack initiation, growth, and interaction. Whereas the greater the geometric homogeneity, the more uniform the internal stress distribution

Table 2. Interface/Contact Properties for Lac du Bonnet Granite and Äspö Diorite^a

| Index | Normal Stiffness, Kn (N/m) | | Kn/Ks | | Cohesion for Both LdB and AD (MPa) | Friction (°) | | Tensile Strength for Both LdB and AD (MPa) |
|-------------|----------------------------|----------|-------|----|------------------------------------|--------------|----|--|
| | LdB | AD | LdB | AD | | LdB | AD | |
| 1 | 9.28E+13 | 1.74E+14 | | | | | | |
| 2 | 8.56E+13 | 2.90E+14 | | | | | | |
| 3 | 1.24E+14 | 2.49E+14 | | | | | | |
| 4 | 1.49E+14 | 1.01E+14 | | | | | | |
| 5 | 9.20E+13 | 1.04E+15 | | | | | | |
| 6 | 1.29E+14 | 6.36E+14 | | | | | | |
| 7 | 1.51E+14 | 1.37E+14 | | | | | | |
| 8 | 2.55E+14 | 4.77E+14 | | | | | | |
| 9 | 3.13E+14 | 1.26E+14 | | | | | | |
| 10 | 4.70E+14 | 7.55E+13 | | | | | | |
| All Indices | | | 1.5 | 3 | 40 | 27 | 32 | 14.4 |

^aLdB, Lac du Bonnet; AD, Äspö Diorite.

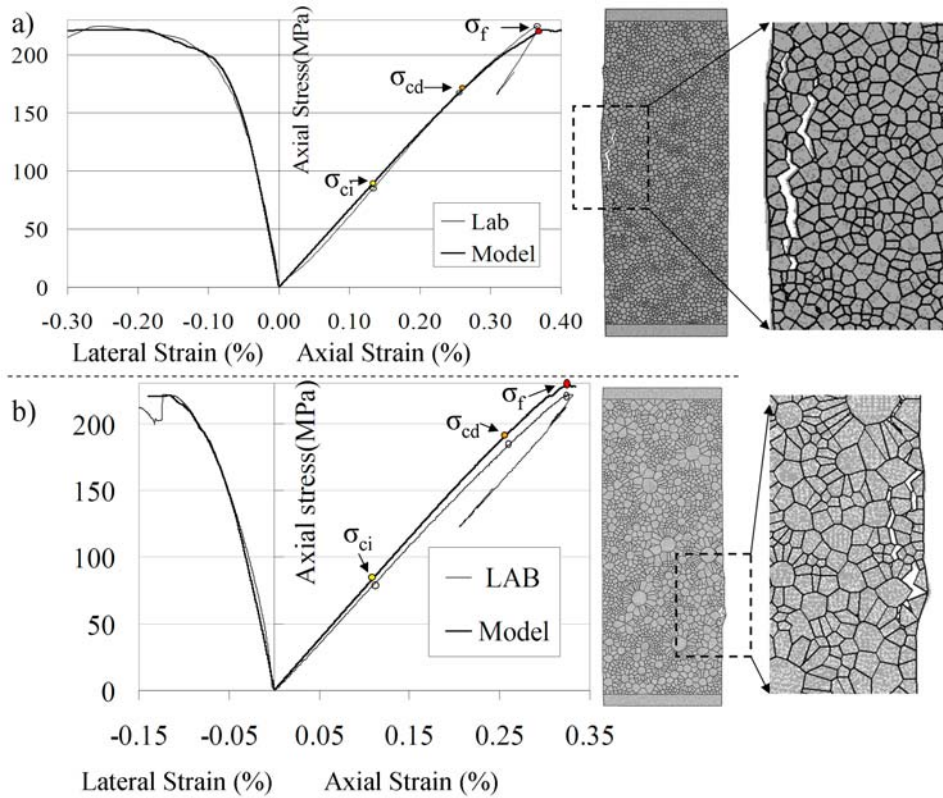


Figure 9. Calibrated stress strain response with lab test data for (a) LdB granite and (b) AD. The drawings at the right show the damage pattern of specimen.

which in our samples leads to higher compressive strength.

5. Effect of Heterogeneity on Sample Behavior

[32] The calibrated models for granite and diorite take into account the grain-geometric heterogeneity, strength heterogeneity, and contact heterogeneity. The effect of these heterogeneities on the extensile stress and extension cracks distribution will be examined.

[33] Figures 14 and 15 show the extensile stress distribution within the mineral grain and the distributed tensile cracks along grain boundaries for LdB granite and AD. Their macroscopic responses are very similar. Before crack initiation, both samples exhibit an elastic behavior and almost no tensile cracks form. After crack initiation, tensile cracks accumulate systematically and, are distributed

Table 4. Calibrated Properties and Error

| Item | Model | LAB | Error (%) |
|---|--|-----------------------|-----------|
| <i>Young's Modulus (E) (GPa)</i> | | | |
| LdB | 67 | 70 | -4 |
| AD | 76.3 | 73.6 | +3.53 |
| <i>Possion's Ratio</i> | | | |
| LdB | 0.217 | 0.22 | -1 |
| AD | 0.253 | 0.27 | -4.53 |
| <i>Crack-Initiation Stress σ_{ci} (MPa)</i> | | | |
| LdB | 95(0.14% of stain, 43% of peak) | 91 (41% peak) | +4 |
| AD | 92.7 (0.12% of strain 40.6% of peak) | 89.2 (40% of peak) | +3.92 |
| <i>Crack Damage Stress σ_{cd} (MPa)</i> | | | |
| LdB | 173 (0.26% of strain, 78% of peak) | 169 (75% of peak) | +2 |
| AD | 193.2 (0.26% of strain, 84.7% of peak) | 189.2 (85.2% of peak) | +2.11 |
| <i>Peak Strength σ_f (MPa)</i> | | | |
| LdB | 221 | 224 | -1 |
| AD | 227.9 | 222.1 | +2.61 |

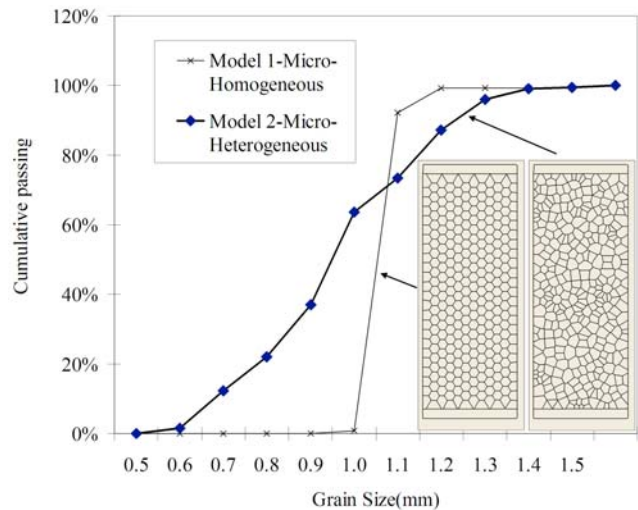


Figure 10. Two models: microhomogenous model and microheterogeneous model. Both models have mean grain size but different grain size distribution which results in different grain-shape distribution using Voronoi diagram.

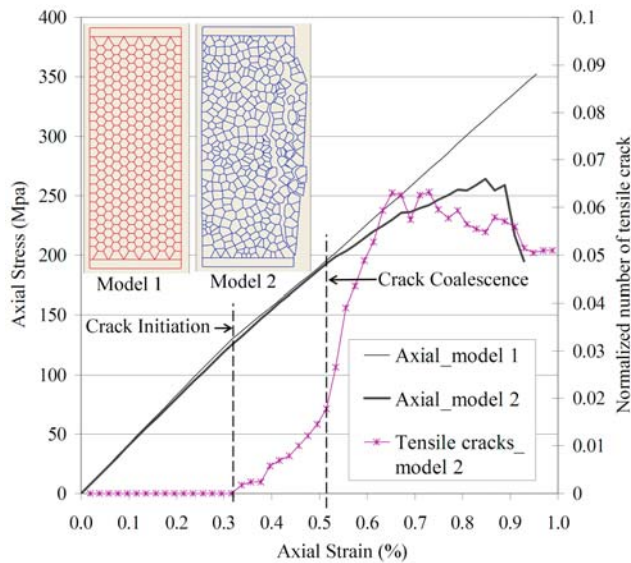


Figure 11. Axial stress and axial strain response for homogeneous model 1 and heterogeneous model 2.

axially aligned throughout the specimen. The development of these axially oriented tensile cracks causes the sample to laterally dilate while axial shortening occurs, i.e., extension cracking. As the load is increased, the cracks interact to form continuous mesoscopic tensile cracks until the peak load is reached. Macroscopic failure in these models occurred near the edge of the sample where the confinement is reduced in these 2-D models (see Figure 9). It should also be noted that because this model cannot accommodate transgranular cracking, the length of the cracks above the stress required for crack coalescence is likely underestimated.

5.1. Effect of Heterogeneity on Stress Distribution

[34] Three characteristic stresses have been identified in the stress-strain curve of the calibrated models (see Figure 9): The crack-initiation stress (σ_{ci}), caused by stable tensile cracking; the stress associated with crack interaction and strain localization (σ_{cd}); and peak strength (σ_f). It has been suggested that the crack-initiation stress and the stress associated with strain localization, sometimes referred to as cracks damage stress, are true material properties in compression testing since they are not affected by the loading rate or the sample size [Martin and Chandler, 1994]. Hence, it is of interest to establish the influence of the various heterogeneities on these stress parameters.

[35] The effect of grain-geometric heterogeneity was discussed above, and the results suggested that the more uniformly grained rock should have a larger crack initiation stress. However, the LdB granite only show a slightly higher initiation stress (91 MPa) compared to the more heterogeneous AD (89 MPa) (see Table 4). In addition to the effect of grain-geometric heterogeneity, the internal microstress distribution is also influenced by the grain modulus variability and strength variability. LdB granite and AD have significantly different strength heterogeneity. For example, the alkali K-feldspar is the most abundant mineral (42%) in the LdB granite sample and more than 45% has a grain size of 3 mm, while the stiffer plagioclase is the dominant mineral

type in AD (see Table 3). Larger abundant grains would likely form the dominant load-bearing skeleton within the granite mass and could therefore dominate the stress development as loading progresses. Thus in one rock the geometric heterogeneity could dominate while in another rock elastic stiffness heterogeneity may dominate. A rock that had both large grain-geometric heterogeneity and large stiffness contrast may have the greatest stress heterogeneity. Such a rock should also have the lowest crack initiation stress. This notion is supported by the findings reported by the Swedish site characterization program of *Svensk Kärnbränslehantering AB (SKB)* [2008] who found that of the various rocks tested at a given site (Forsmark) the coarse grained heterogeneous pegmatite had the lowest crack initiation stress, compared to fine-to-medium grained granites.

[36] Statistical analysis was carried out to examine the detail distribution of tensile and compressive stresses in both models. During uniaxial-strain compression, the axial stress, lateral stress, maximum principal stress (σ_1), and minor principal stress (σ_3) were recorded for every deformable zone of each grain. The contact stress (normal and shear) was also calculated. Figure 16 shows the stress distribution of LdB granite at the crack-initiation loading (95 MPa). While the distribution of principal stress within the grains can be described by a normal distribution (see Figures 16a and 16b), the stress distribution for the contacts approximately fit a bimodal distribution (see Figure 16c). A similar stress distribution was observed in the AD sample.

[37] The coefficient of variation (COV), the standard deviation to the mean ($sd/mean$) of the fitted normal distribution, was used to demonstrate the deviation of stress distribution and concentration [Zhang *et al.*, 2005]. The COV of the axial stress for granite and diorite is compared in Figure 17. Both exhibit a similar trend except the more heterogeneous diorite has higher COV values. The value of COV increases with increasing the strain. At the first stage, the COV is relatively small and remains constant reflecting similar stress distributions during the initial stage of compression. After crack initiation, the COV starts to gradually increase until crack coalescence occurs, after which it increases dramatically.

[38] It can be seen from Figures 14 and 15 that the distribution of large lateral extension stress (for example, >10 MPa), caused by the heterogeneity of rocks is extremely local for stress levels below crack coalescence and interaction. It appears that initial crack growth has little effect on the axial transmission of stress and does not significantly disturb the rest of the sample. Similar findings were reported by Diederichs [2000]. However, when the microcracks start interacting, the axial stress is significantly disturbed which in turn affects the distribution of lateral extension stress (see Figure 17). The stress associated with crack coalescence and interaction may indicate the transition to a different state of compressive stress distribution, which ultimately causes the sample to yield. This state change could then be linked to crack density rather than stress magnitude. The advances in computed imaging tomography combined with acoustic emission monitoring may provide an alternative method of assessing crack density, but this technology is still evolving. Numerical models today still provide a convenient means of quantifying crack density.

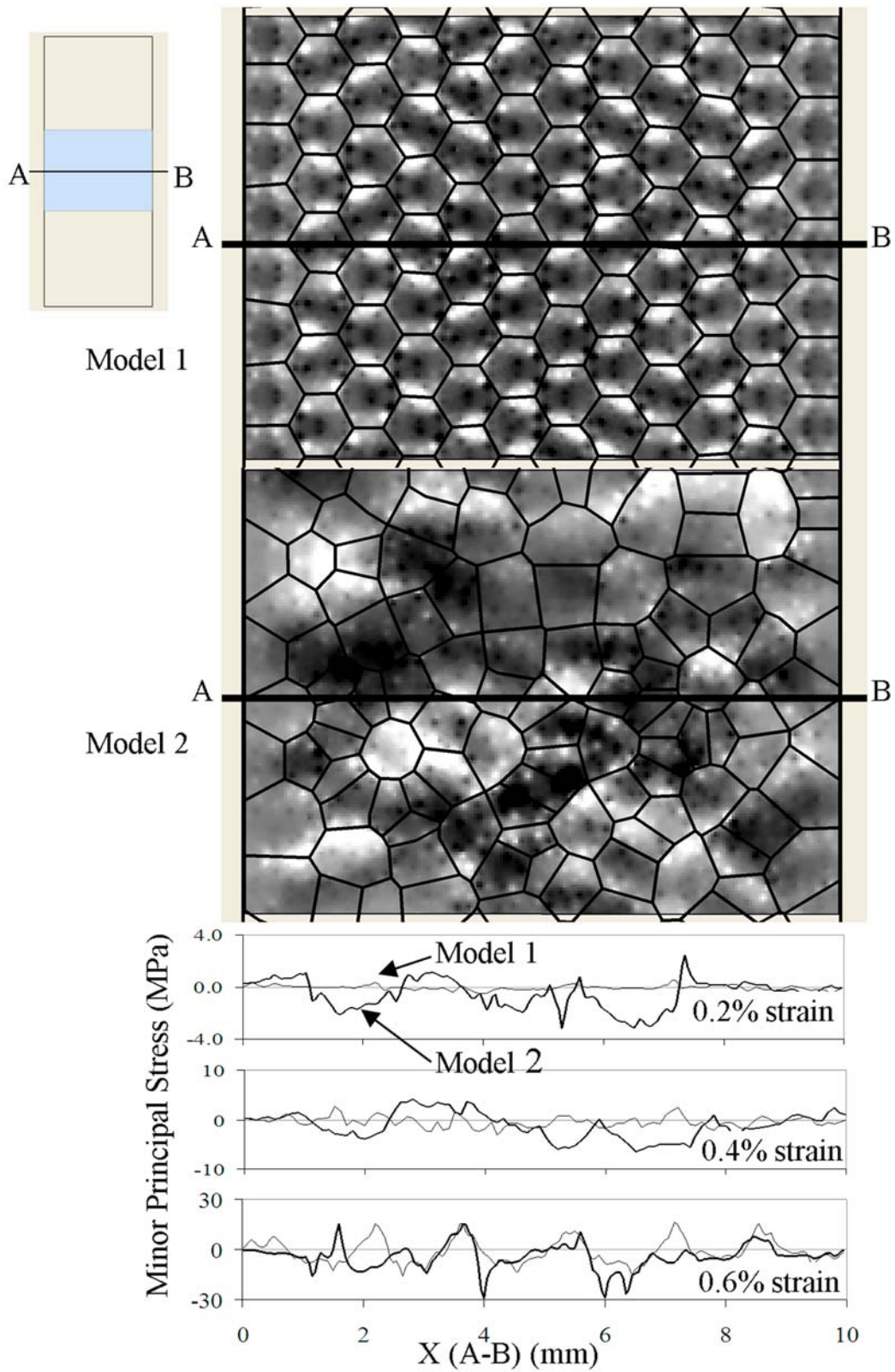


Figure 12. Minor principal stress distribution in the middle part of models and along scan line A-B. The dark regions indicate tension.

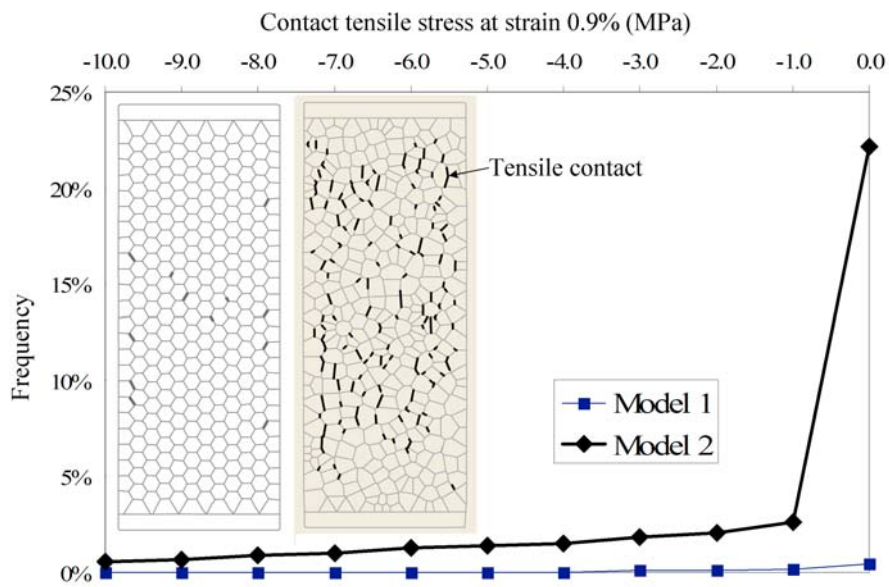


Figure 13. Statistical analysis of contacts on extension.

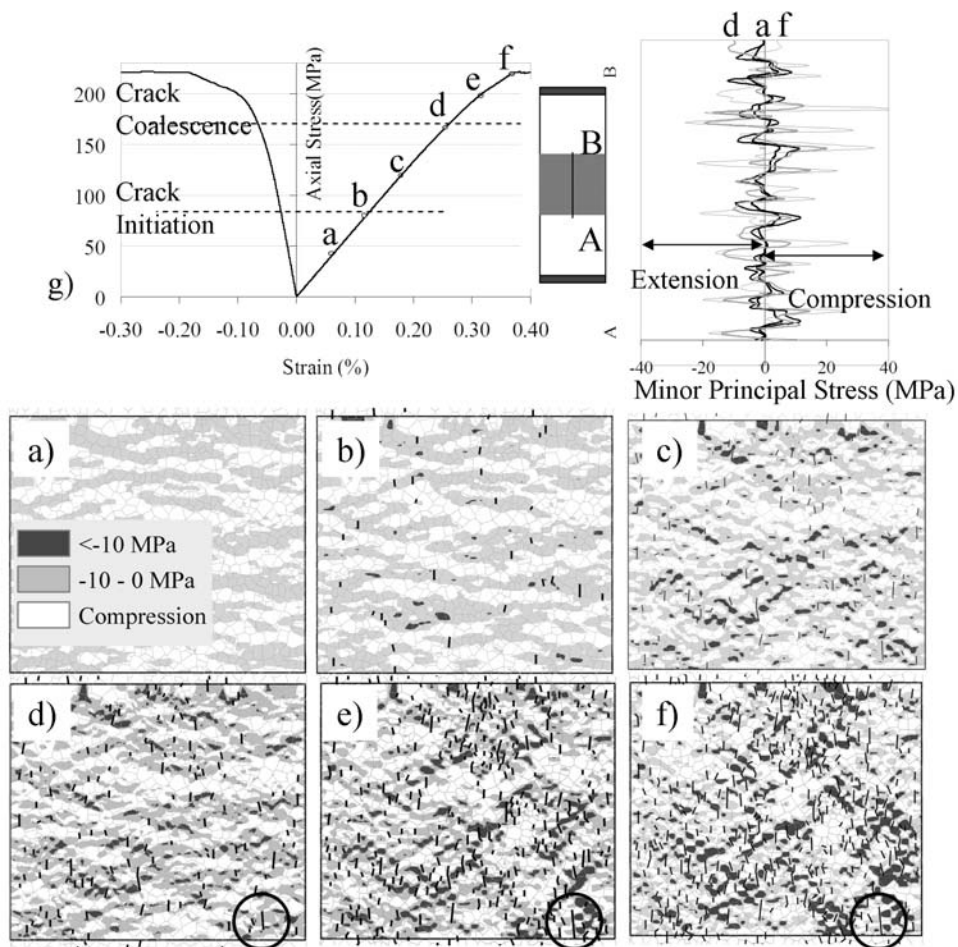


Figure 14. The predicted evolution of distribution of extensile stress and extension cracks in Lac du Bonnet granite. Figure 14g (left) provides locations for Figures 14a–14f. Tiny cracks are not shown (for example, crack shorter than 0.3 mm). Note the crack growth located in the center of the circle.

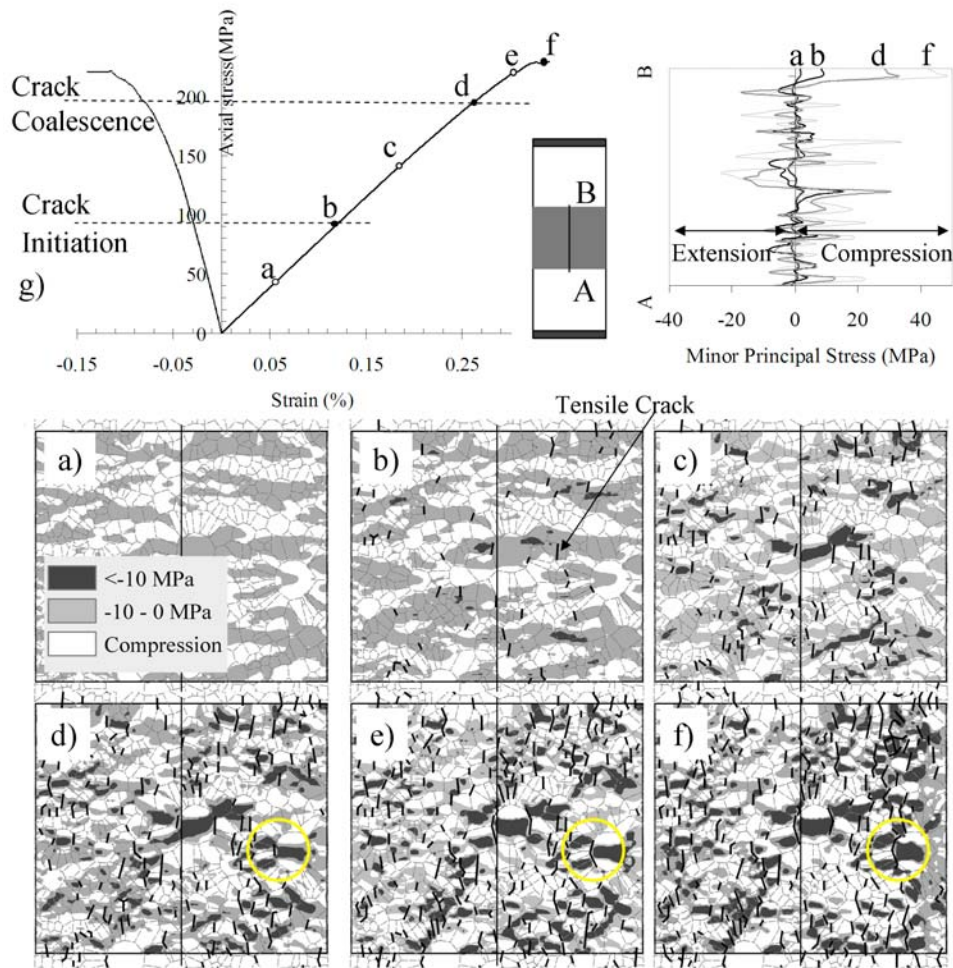


Figure 15. The predicted evolution of distribution of extensile stress and extension cracks in Äspö Diorite. Figures 15g (left) provides locations for Figures 15a–15f. Tiny cracks were not shown. Note the crack growth located in the center of the circle.

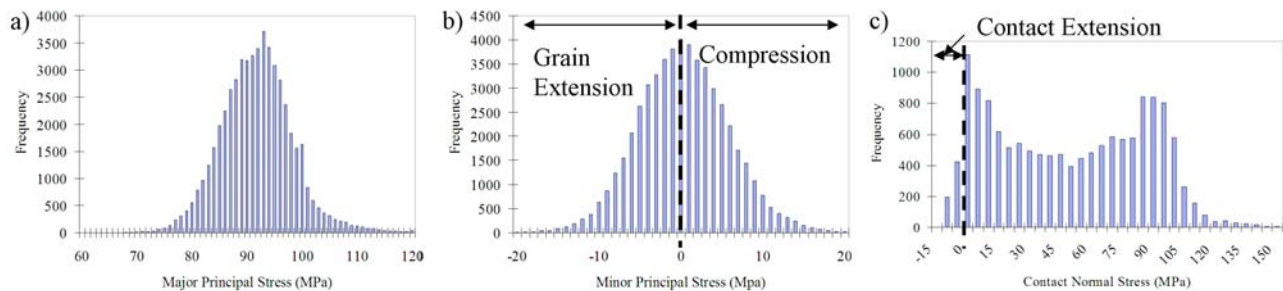


Figure 16. Stress distribution at the crack-initiation stress level for LdB granite.

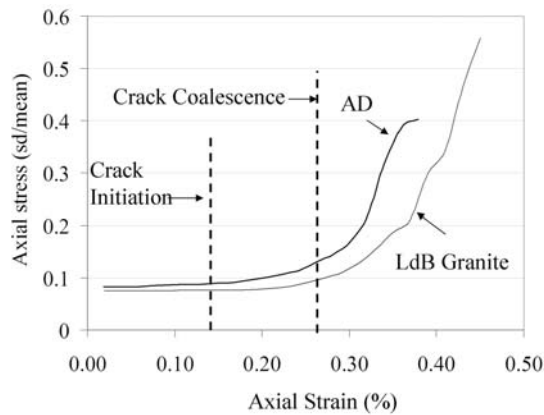


Figure 17. The ratio of standard deviation to mean axial stress (sd/mean), also called coefficient of variation (COV), for AD and LdB granite.

5.2. Heterogeneity and Crack Density

[39] It has been established that extensile crack damage starting at the grain scale is the primary mechanism of rupture for rocks in compression [Wong, 1982a; Myer *et al.*, 1992; Moore and Lockner, 1995]. As shown above, the nucleation of new extension cracks is closely related to the nonhomogeneity of tensile stress distribution induced by microstructure heterogeneity. The process of cracking from the crack-initiation level to the crack-coalescence level is primarily the process of initiating new tensile cracks. The axial stress level where the total volumetric strain changes from overall contraction to dilation marks the beginning of crack interaction and coalescence (d in Figures 14 and 15). It generally occurs at axial stress levels between 70% and 85% of the short-term peak strength. It is at this stress level that the axial strain departs from linearity. Hallbauer *et al.* [1973] concluded this stage is characterized by the most significant structural change during loading with the density of microcracks increasing by about sevenfold. Crack density is determined at this stage in our models to examine how macroscale dilation (volumetric strain reversal) and strain localization are initiated.

[40] The crack density was calculated using the definition by Bristow [1960] in which the summation of square of crack length is divided by the area of interest. The dilation for tensile crack dilation was measured throughout the middle one third of the sample. The evolution of crack density and average dilation for tensile cracks are shown in Figure 18. Both samples clearly show a change in crack density as the load increases. AD shows the greatest changes in crack density and dilation after crack interaction commences. While Hallbauer *et al.* [1973] observed a sevenfold increase in crack density, which is similar for AD, we only observe about a fourfold increase in LdB granite. Our results are likely biased by the constraint that our model does not allow transgranular cracking. Tromans and Meech [2002, 2004] showed that the fracture toughness of grain boundary cracks is lower than that of intragranular cracks by about 10%. Their results suggest that while the density of both grain boundary and intragranular cracking is similar, the grain boundary cracks should initiate first. Nonetheless it is clear from Figure 18 that significant internal changes to the sample occur once crack interaction

commences, suggesting that a critical crack density controls the initiation of strain localization and likely the peak strength of the sample.

[41] It is well known that the peak strength of rocks in laboratory tests is influenced by sample size, width-to-height ratio, and loading rate [e.g., see Hudson *et al.*, 1972]. The numerical modeling described in this paper offers a methodology for linking damage evolution and the observations made in those laboratory tests.

6. Conclusions

[42] The GBM-UDEC model was created to represent the microstructure of brittle rock by taking into account grain-scale geometric heterogeneity, elastic heterogeneity, and contact heterogeneity. The grain-scale heterogeneity was captured by modifying a voronoi polygon generator. The discrete element program was then used to examine the effect of grain-scale heterogeneity on the stress-strain response of two samples.

[43] The grain-scale heterogeneities were shown to have controlling effects on the distribution of tensile stress and associated extension cracks. The grain-geometric heterogeneity was shown to have the most significant impact on peak strength for the two granites investigated. The heterogeneity in grain type played a secondary role.

[44] The compressive strength a sample achieves is defined by extent of tension cracking, and this is controlled by ability of the microgeometric heterogeneity and strength heterogeneity of the mineral grains to generate tensile stress. Our findings suggest that the crack damage stress, i.e., the compressive stress required to initiate the formation of macroscale dilation and strain localization, is controlled by crack density.

[45] The GBM-UDEC model is a research tool to aid in the understanding of brittle failure processes. The model suggests that sample heterogeneity is a primary factor in controlling the stress-strain response measured in laboratory samples. The peak compressive strength, which is normally reported in laboratory test results, does not capture the damage process observed in laboratory testing or in the numerical models used to simulate rock behavior. Calibrating numerical models only to the peak strength or macroscale stiffness may lead to erroneous conclusions.

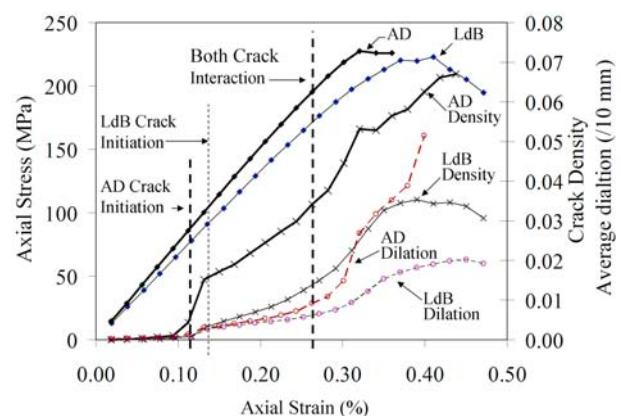


Figure 18. Evolution of tensile crack density and average dilation of tensile crack for LdB granite and AD.

[46] **Acknowledgments.** The authors wish to acknowledge the contributions from the Swedish Nuclear Fuel and Waste Management Co. (SKB, Stockholm) and the Decovalex Project (Decovalex 2011). The support of the Natural Sciences and Engineering Council of Canada, One Hundred Talents Program of Chinese Academy of Sciences, and National Key Technology R&D Program of China (2008BAK50B05) are also acknowledged.

References

- Åkesson, U. (2008), Characterisation of micro cracks caused by core-disking, *SKB Rep. P-08-103*, 43 pp., Swed. Nuclear Fuel and Waste Manage. Co., Stockholm.
- Andersson, J. C. (2007), Äspö pillar stability experiment: Rock mass response to coupled mechanical thermal loading, Ph.D. thesis, R. Inst. of Technol., Stockholm.
- Bass, D. J. (1995), Elasticity of minerals, glasses and melts, in *Mineral Physics and Crystallography, Ref. Shelf Ser.*, vol. 2, edited by T. J. Ahrens, pp. 45–63, AGU, Washington, D. C.
- Blair, S. C., and N. G. W. Cook (1998a), Analysis of compressive fracture in rock using statistical techniques: Part I, A non-linear rule-based model, *Int. J. Rock Mech. Min. Sci.*, 35, 837–848, doi:10.1016/S0148-9062(98)00008-4.
- Blair, S. C., and N. G. W. Cook (1998b), Analysis of compressive fracture in rock using statistical techniques: Part II. Effect of microscale heterogeneity on macroscopic deformation, *Int. J. Rock Mech. Min. Sci.*, 35, 849–861, doi:10.1016/S0148-9062(98)00009-6.
- Brace, W. F. (1961), Dependence of fracture strength of rocks on grain size, in *Proceedings of the 4th Symposium on Rock Mechanics*, edited by H. L. Hartmann, pp. 99–103, Penn. State Univ., University Park.
- Brace, W. F., B. W. Paulding, and C. Scholz (1966), Dilatancy in the fracture of crystalline rocks, *J. Geophys. Res.*, 71(16), 3939–3953.
- Bristow, J. R. (1960), Microcracks and the static and dynamic elastic constants of annealed and heavily cold-work metals, *Br. J. Appl. Phys.*, 11, 81–85, doi:10.1088/0508-3443/11/2/309.
- Cho, N., C. D. Martin, and D. S. Segol (2007), A clumped particle model for rock, *Int. J. Rock Mech. Min. Sci.*, 44, 997–1010, doi:10.1016/j.ijrmm.2007.02.002.
- Cundall, P., and O. Strack (1979), A discrete numerical model for granular assemblies, *Geotechnique*, 29(1), 47–65, doi:10.1680/geot.1979.29.1.47.
- Damjanac, B., M. Board, M. Lin, D. Kicker, and J. Leem (2007), Mechanical degradation of emplacement drifts at Yucca Mountain—A modeling case study Part II: Lithophysal rock, *Int. J. Rock Mech. Min. Sci.*, 44, 351–367, doi:10.1016/j.ijrmm.2006.07.010.
- Diederichs, M. S. (2000), Instability of hard rockmasses: The role of tensile damage and relaxation, Ph.D. thesis, 566 pp., Univ. of Waterloo, Waterloo, Ont., Canada.
- Diederichs, M. S. (2003), Rock fracture and collapse under low confinement conditions, *Rock Mech. Rock Eng.*, 36, 339–381, doi:10.1007/s00603-003-0015-y.
- Eberhardt, E., D. Stead, B. Stimpson, and R. S. Read (1998), Identifying crack initiation and propagation thresholds in brittle rock, *Can. Geotech. J.*, 35(2), 222–233, doi:10.1139/cgj-35-2-222.
- Eberhardt, E., B. Stimpson, and D. Stead (1999), Effects of grain size on the initiation and propagation thresholds of stress-induced brittle fractures, *Rock Mech. Rock Eng.*, 32, 81–99, doi:10.1007/s0060300050026.
- Exadaktylos, G. E., and I. Vardoulakis (2001), Microstructure in Linear elasticity and scale effects: A reconsideration of basic rock mechanics and rock fracture mechanics, *Tectonophysics*, 335, 81–109, doi:10.1016/S0040-1951(01)00047-6.
- Fairhurst, C., and N. G. W. Cook (1966), The phenomenon of rock splitting parallel to the direction of maximum compression in the neighborhood of a surface, paper presented at 1st Congress, Int. Soc. of Rock Mech., Lisbon.
- Fonseka, G. M., S. A. F. Murrell, and P. Barnes (1985), Scanning electron microscope and acoustic emission studies of crack development in rocks, *Int. J. Mech. Min. Sci. Geomech. Abstr.*, 22, 273–289, doi:10.1016/0148-9062(85)92060-1.
- Fredrich, J., B. Evans, and T.-F. Wong (1990), Effects of grain size on brittle and semi-brittle strength, implications for micromechanical modelling of failure in compression, *J. Geophys. Res.*, 95(B7), 10,907–10,920, doi:10.1029/JB095iB07p10907.
- Fredrich, J. T., B. Menendez, and T.-F. Wong (1995), Imaging the pore structure of geomaterials, *Science*, 268, 276–279, doi:10.1126/science.268.5208.276.
- Gallagher, J. J., Jr., M. Friedman, J. Handin, and G. M. Sowers (1974), Experimental studies relating to microfracture in sandstone, *Tectonophysics*, 21, 203–247, doi:10.1016/0040-1951(74)90053-5.
- Hallbauer, D. K., H. Wagner, and N. G. W. Cook (1973), Some observations concerning the microscopic and mechanical behaviour of quartzite specimens in stiff, triaxial compression tests, *Int. J. Mech. Min. Sci. Geomech. Abstr.*, 10, 713–726, doi:10.1016/0148-9062(73)90015-6.
- Hudson, J. A., E. T. Brown, and C. Fairhurst (1972), Shape of the complete stress-strain curve for rock, in *Proceedings of the 13th U.S. Symposium on Rock Mechanics*, edited by E. Cording, pp. 773–795, Am. Soc. of Civ. Eng., New York.
- Kelly, D. D., D. C. Peck, and R. S. James (1994), Petrography of granitic samples from the 420 m level of the Underground Research Laboratory, Pinawa, Manitoba, report, Laurentian Univ., Sudbury, Ont., Canada.
- Kranz, R. L. (1983), Microcracks in rocks: A review, *Tectonophysics*, 100, 449–480, doi:10.1016/0040-1951(83)90198-1.
- Lajtai, E. Z. (1998), Microscopic fracture processes in a granite, *Rock Mech. Rock Eng.*, 31, 237–250, doi:10.1007/s006030050023.
- Lampinen, H. (2006), Äspö pillar stability experiment: Detailed geological mapping of the pillar blocks, *SKB Rep. IPR-05-24*, 67 pp., Swed. Nuclear Fuel and Waste Manage. Co., Stockholm.
- Li, H., K. Li, G. Subhash, L. J. Kecskes, and R. J. Dowding (2006), Micromechanical modeling of tungsten-based bulk metallic glass matrix composites, *Mater. Sci. Eng. A*, 429, 115–123.
- Martin, C. D., and N. A. Chandler (1994), The progressive fracture of Lac du Bonnet granite, *Int. J. Mech. Min. Sci. Geomech. Abstr.*, 31, 643–659, doi:10.1016/0148-9062(94)90005-1.
- Martin, C. D., R. S. Read, and J. B. Martino (1997), Observations of brittle failure around a circular test tunnel, *Int. J. Rock Mech. Min. Sci.*, 34, 1065–1073, doi:10.1016/S0148-9062(97)00296-9.
- Mavko, G., T. Mukerji, and J. Dvorkin (2003), *The Rock Physics Handbook: Tools for Seismic Analysis of Porous Media*, Cambridge Univ. Press, New York.
- Moore, D. E., and D. A. Lockner (1995), The role of microcracking in shear-fracture propagation in granite, *J. Struct. Geol.*, 17, 95–114, doi:10.1016/0191-8141(94)E0018-T.
- Myer, L. R., J. Kemeny, N. G. W. Cook, R. Ewy, R. Suarez, and Z. Zheng (1992), Extensive cracking in porous rock under differential compressive stress, *Appl. Mech. Rev.*, 45, 263–280, doi:10.1115/1.3119758.
- Nygårds, M., and P. Gudmundson (2002), Micromechanical modeling of ferritic/pearlitic steels, *Mater. Sci. Eng. A*, 325, 435–443.
- Olsson, W. A., and S. S. Peng (1976), Microcrack nucleation in marble, *Int. J. Rock Mech. Min. Sci.*, 13, 53–59.
- Potyondy, D. O., and P. A. Cundall (1998), Modeling notch-formation mechanisms in the URL Mine-by Test Tunnel using bonded assemblies of circular particles, *Int. J. Mech. Min. Sci. Geomech. Abstr.*, 35, 510–511, doi:10.1016/S0148-9062(98)00083-7.
- Potyondy, D. O., and P. A. Cundall (2004), A bonded-particle model for rock, *Int. J. Rock Mech. Min. Sci.*, 41, 1329–1364, doi:10.1016/j.ijrmm.2004.09.011.
- Staub, I., and J. C. Andersson (2004), Äspö pillar stability experiment geology and mechanical properties of the rock in TASQ, *SKB Rep. R-04-01*, Svensk Kärnbränslehantering AB, Stockholm.
- Svensk Kärnbränslehantering AB (SKB) (2008), Site description of Forsmark at completion of the site investigation phase, SDM-site Forsmark, *Tech. Rep. TR-08-05*, Stockholm.
- Tang, C. A. (1997), Numerical simulation on progressive failure leading to collapse and associated seismicity, *Int. J. Rock Mech. Min. Sci.*, 34, 249–262, doi:10.1016/S0148-9062(96)00039-3.
- Tapponier, P., and W. F. Brace (1976), Development of stress induced microcracks in Westerly granite, *Int. J. Mech. Min. Sci. Geomech. Abstr.*, 13, 103–112, doi:10.1016/0148-9062(76)91937-9.
- Tromans, D., and J. A. Meech (2002), Fracture toughness and surface energies of minerals: Theoretical estimates for oxides, sulphides, silicates and halides, *Miner. Eng.*, 15, 1027–1041, doi:10.1016/S0892-6875(02)00213-3.
- Tromans, D., and J. A. Meech (2004), Fracture toughness and surface energies of minerals: Theoretical estimates for oxides, sulphides, silicates and halides, *Miner. Eng.*, 17, 1–15, doi:10.1016/j.mineng.2003.09.006.
- Van de Steen, B., A. Vervoort, J. A. L. Napier, and R. J. Durrheim (2003), Implementation of a flaw model to the fracturing around a vertical shaft, *Rock Mech. Rock Eng.*, 36, 143–161, doi:10.1007/s00603-002-0040-2.
- Wong, T. F. (1982a), Shear fracture of Westerly granite from post failure behaviour, *J. Geophys. Res.*, 87(B2), 990–1000, doi:10.1029/JB087iB02p00990.
- Wong, T. F. (1982b), Micromechanics of faulting in Westerly granite, *Int. J. Mech. Min. Sci. Geomech. Abstr.*, 19, 49–64, doi:10.1016/0148-9062(82)91631-X.
- Wong, R. H. C., K. T. Chau, and P. Wang (1996), Microcracking and grain size effect in Yuen Long marbles, *Int. J. Rock Mech. Min. Sci.*, 33, 479–485, doi:10.1016/0148-9062(96)00007-1.
- Wong, T. F., R. H. C. Wong, K. T. Chau, and C. A. Tang (2006), Microcrack statistics, Weibull distribution and micromechanical modeling of compressive failure in rock, *Mech. Mater.*, 38, 664–681, doi:10.1016/j.mechmat.2005.12.002.

Zavattieri, P. D., P. V. Raghuram, and H. D. Espinosa (2001), A computational model of ceramic microstructures subjected to multi-axial dynamic loading, *J. Mech. Phys. Solids*, 49, 27–68, doi:10.1016/S0022-5096(00)00028-4.

Zhang, K. S., M. S. Wu, and R. Feng (2005), Simulation of microplasticity-induced deformation in uniaxially strained ceramics by 3-D Voronoi

polycrystal modeling, *Int. J. Plast.*, 21, 801–834, doi:10.1016/j.ijplas.2004.05.010.

B. Hu and H. Lan, Department of Civil and Environmental Engineering, University of Alberta, NREF 3-065, Edmonton, AB T6C 2W2, Canada. (bhu3@ualberta.ca; hlan@ualberta.ca)

C. D. Martin, Department of Civil and Environmental Engineering, University of Alberta, NREF 3-071, Edmonton, AB T6C 2W2, Canada. (Derek.martin@ualberta.ca)